American Journal of Engineering and Applied Sciences

Research Article

A Comparative SCAPS-1D Study of Lead-Free $CsSnCl_3$-Based Perovskite SCs Employing Different ETLs

Rony Tota, Shak Mahmudul Hasan, Md. Morsalin, Md. Muien Ahmed Arnob, Tarikul Islam Tasin and Md. Zamil Sultan

Department of Electrical and Electronic Engineering, Hajee Mohammad Danesh Science and Technology University, Dinajpur 5200, Bangladesh

Article history
Received: 03-07-2025
Revised: 19-07-2025
Accepted: 10-04-2026

Corresponding Author:
Rony Tota
Department of Electrical and Electronic Engineering, Hajee Mohammad Danesh Science and Technology University, Dinajpur 5200, Bangladesh
Email: ronytota98@gmail.com

Abstract: Cesium tin chloride ($CsSnCl_3$) has drawn considerable interest as a non-toxic absorber candidate for next-generation photovoltaic devices, offering an attractive combination of affordability, thermal robustness, and competitive conversion performance suitable for clean-energy deployment. In the present work, the photovoltaic behaviour of $CsSnCl_3$-based SCs was numerically examined using the SCAPS-1D software. Three distinct device stacks were constructed by varying the ETL, such as WS_2, C_{60}, and ZnSe, while keeping CBTS fixed as the HTL. To establish optimal operating conditions, the influence of absorber thickness, carrier doping concentration, and bulk defect density was examined alongside the corresponding parameters of the ETL and HTL, with attention paid to four output metrics: PCE, J_{SC}, V_{OC}, and FF. Simulation outcomes confirmed that the choice of ETL exerts a pronounced influence on overall device behaviour. Peak conversion efficiencies of 22.09%, 19.94%, and 21.80% were obtained for the WS_2, C_{60}, and ZnSe-based architectures, respectively. Supplementary investigations addressed the role of series and shunt resistance, Quantum Efficiency (QE), C–V response, operating temperature, interface trap states. The Mott–Schottky characteristics, J-V profiles, and carrier recombination dynamics are also investigated. The numerical outcomes obtained here were benchmarked against earlier reports on $CsSnCl_3$-based devices to evaluate the extent of improvement and the prospects for long-term operation. Taken together, the findings put forward several refined and competitive architectures for high-performing, lead-free $CsSnCl_3$ Solar Cells (SCs), advancing the broader effort toward sustainable and economically viable photovoltaic platforms.

Keywords: Lead-Free Perovskite Solar Cells, Quantum Efficiency, $CsSnCl_3$, Device Optimization, SCAPS-1D, PCE

Introduction

The global energy infrastructure remains heavily anchored to conventional fuels such as coal, gas, and oil, which not only contribute substantially to climate disruption and ecological degradation but also represent a finite resource pool. As a result, the scientific community has intensified its pursuit of alternative pathways centred on renewables, including hydropower, wind, and solar conversion. Among these, sunlight stands out for its sheer abundance: The energy delivered by solar radiation across the planet surpasses the cumulative output of every other renewable resource combined (Chapin et al., 2011). The quantity of solar energy incident on the Earth exceeds world demand, even in highly industrialized economies. Realizing this potential, however, requires effective means of capture, conversion, and storage to overcome the daily and seasonal intermittency of sunlight. Photovoltaic (PV) devices, which transform incident photons directly into electrical current, serve as the front-end technology for harvesting this resource.

SCIENCE Publications

Among the photovoltaic landscape, Perovskite Solar Cells (PSCs) have emerged as a third-generation solution that can compete with established silicon technologies, due to its simple fabrication and low production costs (Song et al., 2017). A common example geometry of device is the planar n-i-p heterojunction, whereby a stack of layers of semiconductors are stacked one-dimensionally. The past decade has seen PSCs being given a lot of scientific attention owing to their dual potential of high conversion efficiencies and low-cost manufacturability (Green et al., 2014; Park, 2015). Although the performance of lead-containing perovskites is impressive, the intrinsic toxicity of Pb has inspired a flood of research aimed at lead-free alternatives (Saliba et al., 2016; Leijtens et al., 2015; Walsh, 2015). It is on this platform that CsSnCl3 has emerged as an attractive absorber, able to provide respectable efficiencies without the need to use lead bearing constituents (Jiang et al., 2020). Of all the types of compositions that are currently being studied to be used in PSCs, cesium tin chloride is particularly unique, as a lead-free solution. In order to enhance the output of the devices, researchers often combine $CsSnCl_3$ with CBTS as the HTL and WS_2 as the ETL.

The conversion performance of these architectures is directly related to the bulk defect concentration of the absorber, a parameter that can be optimised in order to improve the behaviour of the device. Simulation packages like SCAPS are often used to estimate SC response to various operating conditions to prove how defect density varies affect the operation of a device. Such modelling undertakings are aimed at developing the operational stability and conversion capability of PSCs and increasing its use in renewable energy systems. It is possible to rigorously evaluate the dependence of the photovoltaic figures of merit on the active-layer trap density (Nt) of CsSnCl 3-based devices by sweeping the active-layer trap density (Nt). The simulations affirm that the performance measures increase significantly when the defect density is suppressed. At the lowest examined defect concentration of 10^{11} cm^{-3}, the device delivers a FF of 81.97%, a J_{SC} of 26.25 mA/cm^2, an V_{OC} of 1.03 V, and a PCE of 22.09% (Ullah et al., 2019). The numerical analysis was performed using the SCAPS package, which is best suited to the analysis of stacked semiconductor architectures and the resulting trends provide valuable insight into how the operation of $CsSnCl_3$ PSCs depends on trap density.

According to a report provided by Chowdhury et al. (2020) to date laboratory-scale PSCs have reached a verified PCE of 24.2% as of 2020, as reported by the Korea Research Institute of Chemical Technology. In a similar attempt, Hossain et al. reported a single-junction perovskite device in 2021, with a J_{SC} of 21.8 mA/cm^2, a V_{OC} of 1.09 V, an FF of 77, and a PCE of 17.9% (Saidani et al., 2023). Later, Ahmed and co-workers reported a lead-free PSC with 20.19% efficiency in 2022 (Umar et al., 2022). The sum of these contributions supports the conclusion that the reduction of the bulk defect content of CsSnCl 3 absorbers is the key to unlocking high efficiencies. The parameters that determine the behaviour of a device can be disentangled with the help of computational tools such as SCAPS, which can be directed to guide the design of next-generation cells (Simya et al., 2015; Ahmad et al., 2023; Li et al., 2025). Lead-free, CsSnCl3 based, PSCs thus have some real promise of replacing the lead based counterparts as research in this area matures.

Methodology

The proposed PSC architecture is shown schematically in Figure 1, with the layer stack organised as Glass/ITO/ETL/$CsSnCl_3$/CBTS/Au. $CsSnCl_3$ acts as the photoactive absorber within this stack and largely dictates the photovoltaic (PV) response owing to its strong optical absorption profile. The corresponding crystallographic arrangement of $CsSnCl_3$ is presented in Figure 2, while Figure 3 displays the schematic energy-level diagram of the proposed device.

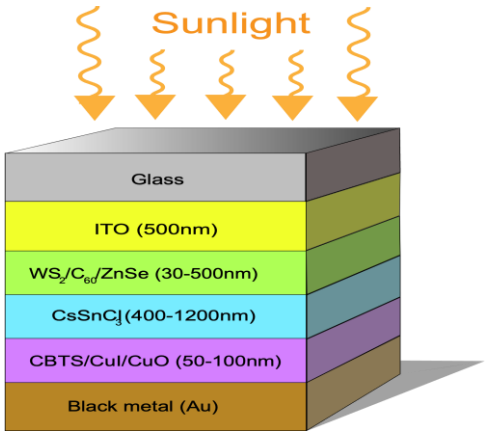

Fig. 1: Layer-stack schematic of the proposed $CsSnCl_3$-based PSC

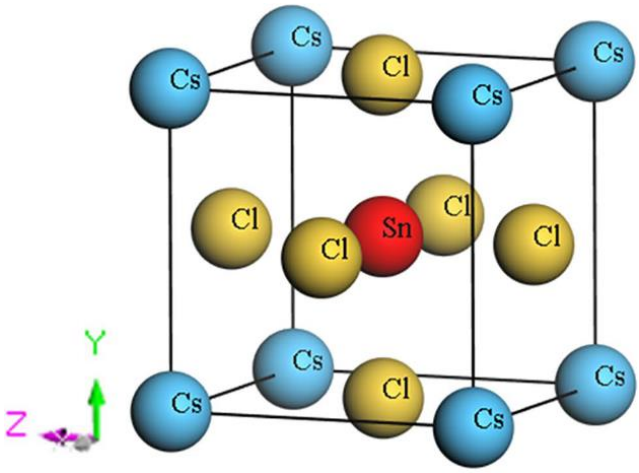

Fig. 2: Optimized crystallographic configuration of the $CsSnCl_3$ perovskite

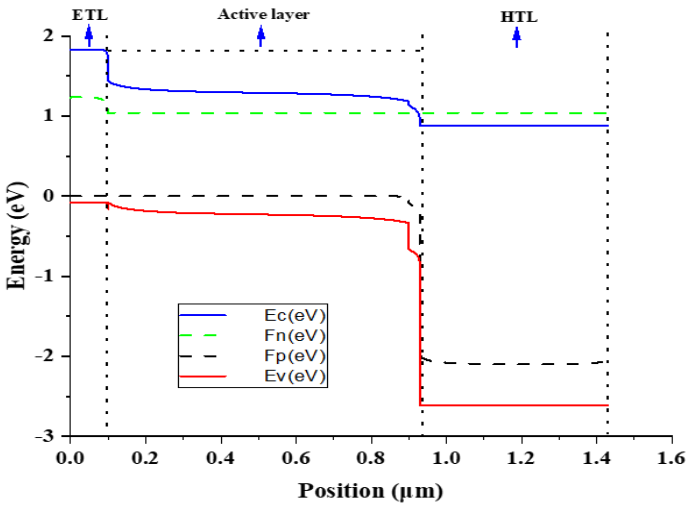

Fig. 3: Schematic energy band alignment of the proposed PSC stack

Within the device geometry, Indium Tin Oxide (ITO) operates as the Transparent Conductive Oxide (TCO), CBTS is assigned the role of HTL, and glass and gold (Au) serve as the front-illumination window and rear electrode, respectively. To probe the role of charge-extraction materials on overall device behaviour, three different ETL candidates were examined: WS_2, C_{60}, and ZnSe. The coupling between the ETL and HTL governs how efficiently photogenerated carriers are transported away from the absorber and collected at the contacts, and therefore directly modulates the principal performance indicators namely the V_{OC}, J_{SC}, FF, and PCE. The V_{OC}, in particular, is dictated by the offset between the Fermi levels of the ETL and the HTL.

All photovoltaic simulations were carried out under standard test conditions of 100 mW/cm² incident power, employing the AM1.5G reference spectrum with the device held at 300 K. To improve overall device output, the series resistance (R_s) and shunt resistance (R_sh) were also tuned. The numerical work was performed using SCAPS-1D (SC Capacitance Simulator), a one-dimensional device-modelling platform developed by Burgelman and colleagues at the Department of Electronics and Information Systems, University of Ghent, Belgium (Niemegeers et al.,1998; Burgelman et al., 2000). SCAPS-1D enjoys widespread adoption across the photovoltaic research community owing to its capability of reliably reproducing both the spectral and electrical signatures of SCs. The complete set of input parameters used for the present thin-film simulations is compiled in Tables 1–3, with the corresponding values drawn from values reported in the previous literature.

Table 1: Simulation input parameters adopted for the TCO, ETL, and absorber layers in this work (Saidani et al., 2023)

Parameters	$CsSnI_3$	C_{60}	WS_2	ZnSe	ITO
X_{th} (nm)	800	30	30	80	500
E_g (eV)	1.52	1.7	1.8	2.9	3.5
χ (eV)	3.9	3.9	3.95	4.09	4
ε_r (relative),	29.4	4.2	13.6	10	9
Nc (cm^{-3})	1×10^{19}	8×10^{19}	1×10^{18}	1.5×10^{18}	2.2×10^{18}
Nv (cm^{-3})	1×10^{19}	8×10^{19}	2.4×10^{19}	1.8×10^{18}	1.8×10^{19}
μ_n ($cm\ s^{-1}$)	1×10^{7}	1×10^{7}	1×10^{7}	1×10^{7}	1×10^{7}
Vn (cm^2/VJ)	2	8×10^{-2}	100	25	20
μ_p ($cm\ s^{-1}$)	1×10^{7}	1×10^{7}	1×10^{7}	1×10^{7}	1×10^{7}
Vp (cm^2/V s)	2	3.5×10^{-3}	100	100	10
N_D (cm^{-3})	0*	1×10^{17}	1×10^{18}	0	1×10^{21}
N_A (cm^{-3})	$1\times10^{15*}$	0	0	1×10^{17}	0
Nt (cm^{-3})	$1\times10^{15*}$	$1\times10^{16*}$	$1\times10^{16*}$	$1\times10^{16*}$	$1\times10^{15*}$

Table 2: Simulation input parameters adopted for the HTL candidates in this work (Saidani et al., 2023)

HTL	CBTS	CuI	CuO
X_{th} (nm)	100	100	50
E_g (eV)	1.9	3.1	1.51
χ (eV)	3.6	2.1	4.07
ε_r (relative),	5.4	6.5	18.1
Nc (cm^{-3})	2.2×10^{18}	2.8×10^{19}	2.2×10^{19}
Nv (cm^{-3})	1.8×10^{19}	1×10^{19}	5.5×10^{15}
μ_n ($cm\ s^{-1}$)	1×10^{7}	1×10^{7}	1×10^{7}
Vn (cm^2/VJ)	30	100	100
μ_p ($cm\ s^{-1}$)	1×10^{7}	1×10^{7}	1×10^{7}
N_D (cm^{-3})	0	0	0
N_A (cm^{-3})	1×10^{18}	1×10^{18}	1×10^{18}
Nt (cm^{-3})	$1\times10^{15*}$	$1\times10^{15*}$	$1\times10^{15*}$

Here, X_{th}: Thickness, E_g: Bandgap, χ: Electron Affinity, N_D: Shallow uniform donor density, ε_r: Dielectric permittivity, μ_p: Hole mobility, N_c: CB effective DOS, Vn: electron thermal velocity, Vp: hole thermal velocity, N_v: VB effective DOS, μ_n: Electron mobility, N_A: Shallow uniform acceptor density and N_t: Defect density

Table 3: Defect parameters assigned to the interfacial layers in this study (Saidani et al., 2023)

Interface	Reference for defect energy level	Total density (cm^{-3}) (integrated overall energies)	Defect type	Capture cross section: Electrons/holes(cm^2)	Energetic distribution
ETL/$CsSnCl_3$	Above the VB maximum	10^{10}	Neutral	10^{-17} 10^{-18}	Single
$CsSnCl_3$ /HTL	Above the VB maximum	10^{10}	Neutral	10^{-18} 10^{-19}	Single

Results and Discussion

The photovoltaic response of the proposed Glass/ITO/ETL/$CsSnCl_3$/CBTS/Au architecture was evaluated by sweeping the principal physical parameters of each functional layer and tracking the resulting changes in V_{OC}, J_{SC}, FF, and PCE. For the baseline configurations, the absorber thickness was held at 800 nm, the acceptor doping in $CsSnCl_3$ was fixed at 10^{18} cm^{-3}, and the bulk trap density was set to 10^{15} cm^{-3}, while the ETL and HTL parameters listed in Tables 1 and 2 were retained as the starting reference. Three device variants were constructed by substituting WS_2, C_{60}, and ZnSe in the ETL position, with CBTS kept fixed as the HTL across all three stacks. The discussion that follows is organised in the conventional sequence adopted in SCAPS literature: First, the influence of the absorber-layer parameters is examined; the analysis then turns to the corresponding parameters of the ETL, followed by those of the HTL; finally, the capacitance, Mott–Schottky, generation–recombination, and comparative figures-of-merit analyses are presented.

Selection of the Charge Transport Layer Combinations

The rationale behind choosing WS_2, C_{60}, and ZnSe as ETL candidates and CBTS as the reference HTL is shortly described. Both WS2 and ZnSe have wide optical bandgaps (1.8 eV and 2.9 eV, respectively) which allow nearly

transparent windows to allow incoming photons to pass through the material, and at the same time provide good conduction-band alignment with $CsSnCl_3$. C_{60} though with a narrower bandgap, was retained in this study as a representative organic ETL with which to compare its behaviour with the inorganic alternatives. CBTS was chosen on the HTL side due to its earth-abundant constituents, characteristic crystal structure, good optical absorption and conduction- and valence-band positions that favourably match the $CsSnCl_3$ absorber and minimise interfacial recombination (Chakraborty et al., 2019; Arumugam et al., 2021). The carrier-transport scheme in the device is a standard heterojunction picture in which incident photons absorbed in $CsSnCl_3$ generate electron-hole pairs, which are subsequently separated by the built-in electrostatic field with electrons drifted towards the ETL/ITO contact and holes towards the CBTS/Au contact. Due to the relatively high diffusion length and low probability of recombination of electrons, the ETL option has a particularly strong impact on the total device output. The summarized results of the simulation in Tables 4 and 5 support this expectation with WS cations providing the highest PCE of all screened ETLs and CBTS surpassing that of the alternative HTLs (CuI, CuO).

Table 4: Optimized photovoltaic figures of merit for $CsSnCl_3$-based devices across the screened ETL and HTL combinations

	PSC Device	PCE (%)	FF (%)	Jsc(mA/cm^2)	Voc (V)
ETL Screening (HTL: CBTS)	ITO/ZnSe/$CsSnCl_3$/CBTS	21.80	81.00	26.24	1.03
	ITO/C_{60}/$CsSnCl_3$/CBTS	19.94	81.74	23.85	1.02
	ITO/WS_2/$CsSnCl_3$/CBTS	22.09	81.97	26.25	1.03
HTL Screening (ETL: WS_2)	ITO/WS_2 /$CsSnCl_3$/CBTS	22.09	81.97	26.25	1.03
	ITO/WS_2/$CsSnCl_3$/CuO	21.98	82.13	26.20	1.02
	ITO/WS_2/$CsSnCl_3$/CuI	20.98	79.48	26.22	1.00

Table 5: Comparison of PV parameters of $CsSnCl_3$ based on HTL

PSC Device	Voc(v)	Jsc(mA/cm^2)	FF (%)	Efficiency (%)
ITO/WS_2/$CsSnCl_3$/CuI	1.00	26.22	79.48	20.98
ITO/WS_2/$CsSnCl_3$/CuO	1.02	26.20	82.13	21.98
ITO/WS_2 /$CsSnCl_3$/CBTS	1.03	26.25	81.97	22.09

Effect of Absorber-Layer Parameters on PV Performance

Influence of Absorber Defect Density (Nt)

Bulk defects in the perovskite absorber serve as Shockley-Read-Hall recombination centres, which shortens the carrier lifetime and reduces the diffusion length, both of which have the immediate effect of reducing the photovoltaic figures of merit. The absorber defect density was thus varied between 10^{11} and 10^{18} cm^{-3} to obtain the trends in η, J_{SC}, V_{OC}, and FF per ETL configuration and this is plotted in Figure 4. At trap densities of below 10^{15} cm -3 all three configurations were able to maintain a relatively stable performance; beyond that threshold, the metrics degraded very quickly. The WS_2-based stack maintained its status as the strongest performer throughout the entire defect-density window, with highest values of about 25% efficiency, JSC of 30 mA/cm^2, V_{OC} of 1.2 V and FF of 80% at the lowest trap concentration. The ZnSe-based device had the next highest, slightly lower output, and the C6O-based device the steepest drop as Nt increased - its efficiency decreased to around 15% and J_{SC}, and V_{OC} fell to approximately 20 mA/cm^2 and 0.9 V, respectively, at the highest trap density. These results confirm anew that defect engineering of the $CsSnCl_3$ layer is an indisputable lever to unlock high-efficiency operation, especially using an organic ETL like C_{60}.

Influence of Absorber Doping Concentration

The acceptor concentration of the $CsSnCl_3$ absorber was systematically swept from 10^{11} to 10^{18} cm^{-3} to investigate how doping levels reshape the device output. As shown in Figure 5, Two distinct regimes emerged from the simulations. In the lightly doped region ($\leq 10^{15}$ cm^{-3}), V_{OC}, J_{SC}, and FF remained largely insensitive to N_A, indicating that the built-in field and carrier collection efficiency were preserved. Above 10^{15} cm^{-3}, however, JSC and FF began to climb appreciably for all three ETLs. At the highest doping level of 10^{18} cm^{-3}, the WS_2-based device delivered J_{SC} of 24.45 mA/cm², closely matched by ZnSe at 24.05 mA/cm², while C_{60} rose more modestly from 19.69 to 21.38 mA/cm² across the swept range. V_{OC}, in contrast, displayed an opposing trend in the heavily doped region, with WS_2 peaking at 26.25 mA/cm² before dropping to 23.46 mA/cm², and ZnSe declining from 26.24 to 22.87 mA/cm². The fill factors evolved similarly: WS_2 and ZnSe stabilised near 1.18 V V_{OC} with FF values of 87.96% and 88.78%, respectively, while C_{60} peaked at FF = 82.15% before slipping at the highest doping levels. These observations underscore the trade-off intrinsic to absorber doping, while moderate enhancements in JSC and FF can be realised, excessive doping introduces additional recombination pathways that erode V_{OC} and limit further efficiency gains.

DOI: 10.3844/ajeassp.2026.73.87

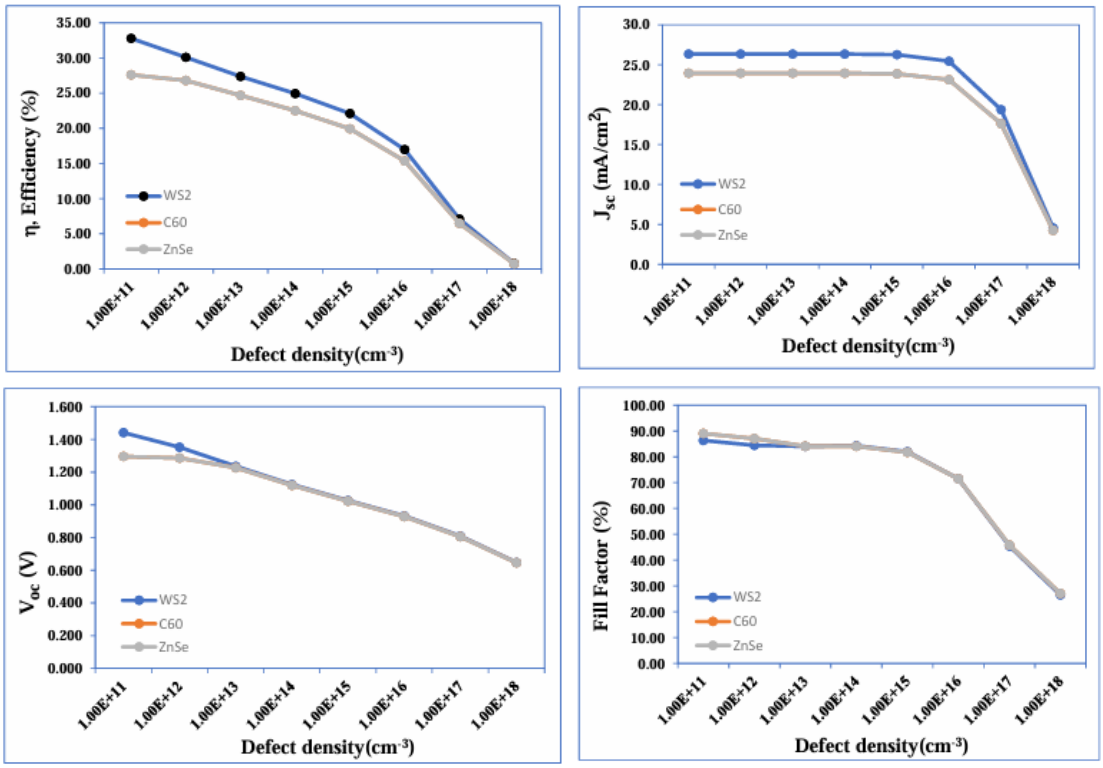

Fig. 4: Variation of PV output parameters as a function of $CsSnCl_3$ absorber defect density with different ETLs

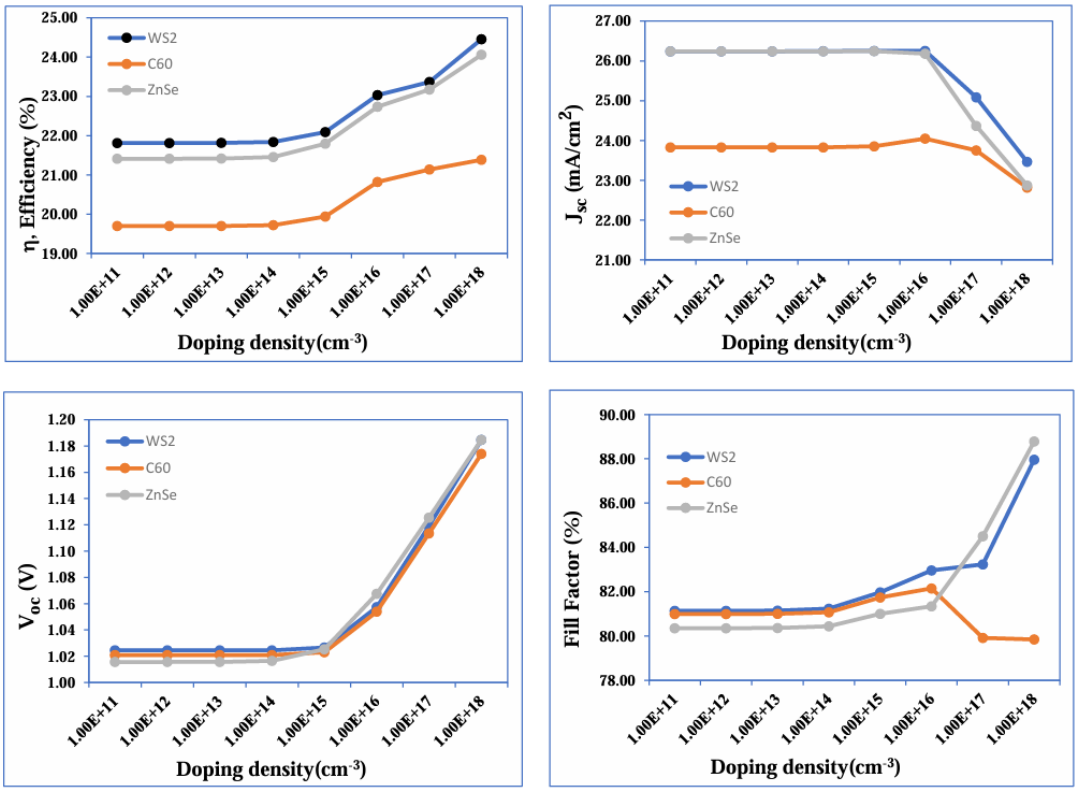

Fig. 5: Variation of PV output parameters as a function of $CsSnCl_3$ absorber doping concentration for the three ETL configurations

Influence of Absorber-Layer Thickness

The thickness of the $CsSnCl_3$ layer was varied between 0.4 µm and 1.2 µm for each device configuration (as shown in Figure 6) to identify the optimum operating window. Photon harvesting improves as the absorber thickens, and the corresponding JSC values reflect this trend, climbing to peak values of 26.87 mA/cm² (WS_2), 26.88 mA/cm² (ZnSe), and 24.44 mA/cm² (C_{60}) at 1.2 µm. Conversely, V_{OC} followed the opposite trajectory: For the WS_2 device, V_{OC} fell from 1.06 V at 0.4 µm to 1.00 V at 1.2 µm, with similar reductions observed for ZnSe and C_{60}. This decline is attributed to enhanced bulk recombination and increased series resistance encountered in thicker films. FF too eroded gradually with thickness from 83.41 to 80.88% in the WS_2 variant, with comparable drops for the other two ETLs. The peak efficiency was reached at 0.8 µm: WS_2 achieved its maximum PCE of 22.09%, ZnSe followed at 21.79%, and C_{60} trailed at 19.94%. Beyond this point, the gains from improved absorption were overwhelmed by recombination and resistive losses, and the optimum absorber thickness was therefore fixed at 0.8 µm for the subsequent analyses.

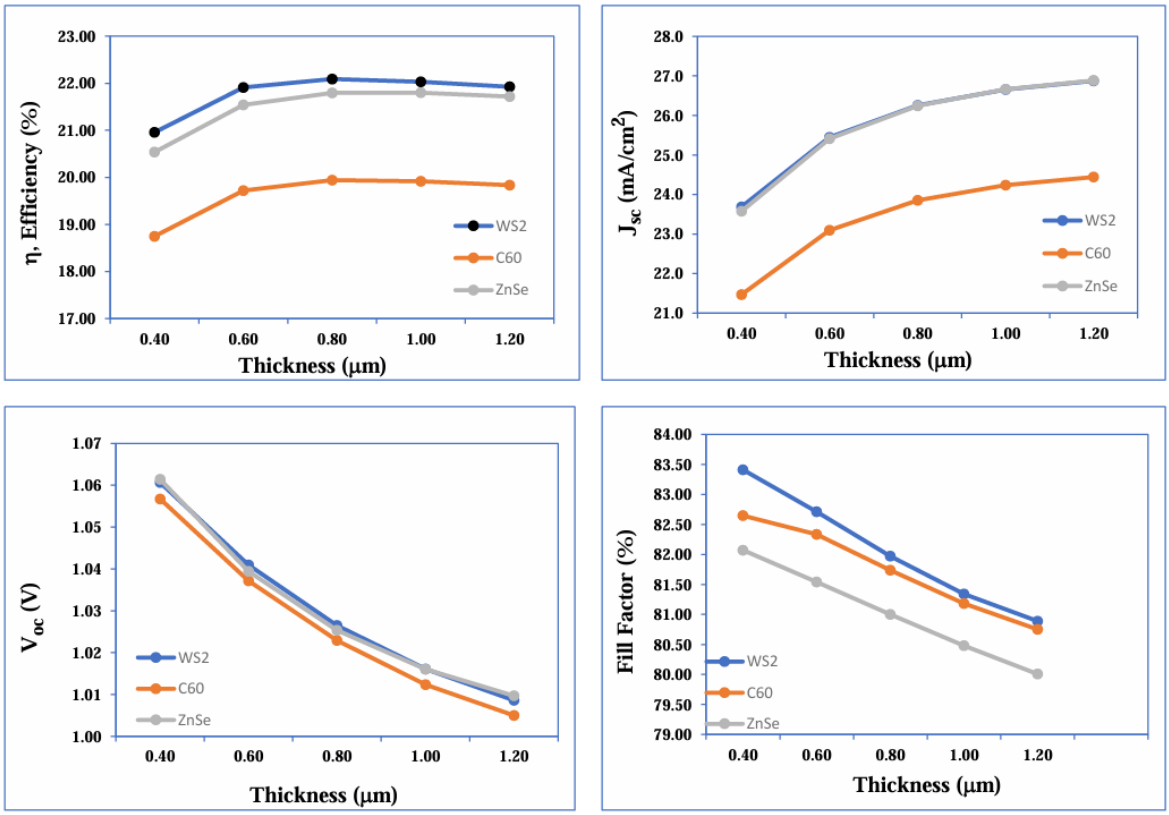

Fig. 6: Dependence of PV output parameters on $CsSnCl_3$ absorber thickness for the three ETL configurations

Effect of ETL Parameters on PV Performance

Influence of ETL Defect Density

Defects within the ETL can serve as recombination centres at the ETL/absorber interface and limit electron extraction. The trap concentrations of WS_2, C_{60}, and ZnSe were varied between 10^{11} and 10^{17} cm^{-3}, with the corresponding device response shown in Figure 7. The inorganic ETLs displayed remarkable tolerance to defect-density variation: WS_2 and ZnSe maintained essentially flat efficiency profiles at 22.09% and 21.79%, respectively, with JSC values held steady at 26.25 and 26.24 mA/cm². C_{60}, in contrast, was distinctly more vulnerable to ETL traps, its efficiency fell from 22.10% to 19.30%, and its JSC dropped from 26.26 to 23.05 mA/cm² across the same range. V_{OC} remained pinned at 1.02 V for all three configurations, while the FF of C_{60} slipped marginally from 81.97% to 81.93%, with WS_2 and ZnSe holding at 81.97% and 81.00%. The contrasting behaviour highlights the superior defect resilience of the wide-bandgap inorganic ETLs and reinforces the structural disadvantage of organic alternatives such as C_{60} when fabrication-induced traps cannot be fully suppressed.

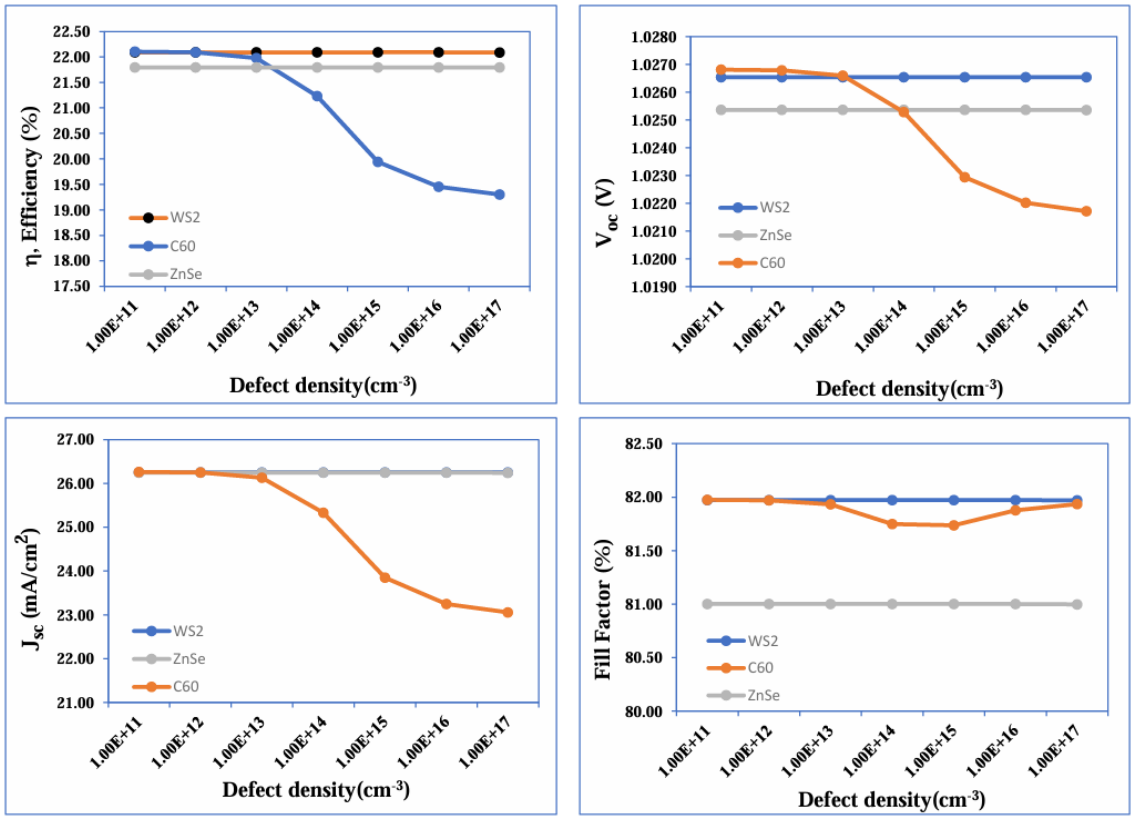

Fig. 7: Variation of PV output parameters with ETL defect density

Influence of ETL Doping Density

To characterize the role of carrier doping within the ETL, the donor concentration was swept from 10^{15} to 10^{20} cm^{-3} for the three configurations as shown in Figure 8.

Increasing the doping level produced modest but consistent enhancements in efficiency for the inorganic ETLs: WS_2 rose from 22.08% to 22.17%, while ZnSe improved from 21.80% to 22.14%. The C_{60}-based device behaved differently, declining marginally from 19.97% to 19.91%, with its JSC falling from 24.73 to 23.67 mA/cm². The JSC values of WS_2 and ZnSe remained nearly invariant at 26.24–26.25 mA/cm², and V_{OC} of all three configurations stabilised around 1.02 V. FF improvements were observed across the board: WS_2 rose from 81.97% to 82.06%, ZnSe climbed from 80.41% to 82.05%, and C_{60} exhibited the largest gain from 79.39% to 82.03%. Although increased doping typically narrows the depletion region near the ETL/absorber interface and strengthens the built-in field, the simultaneous introduction of additional recombination centres in C_{60} accounts for its JSC erosion. The combined behaviour confirms that WS_2 and ZnSe are inherently more compatible with high-doping operation than the organic counterpart.

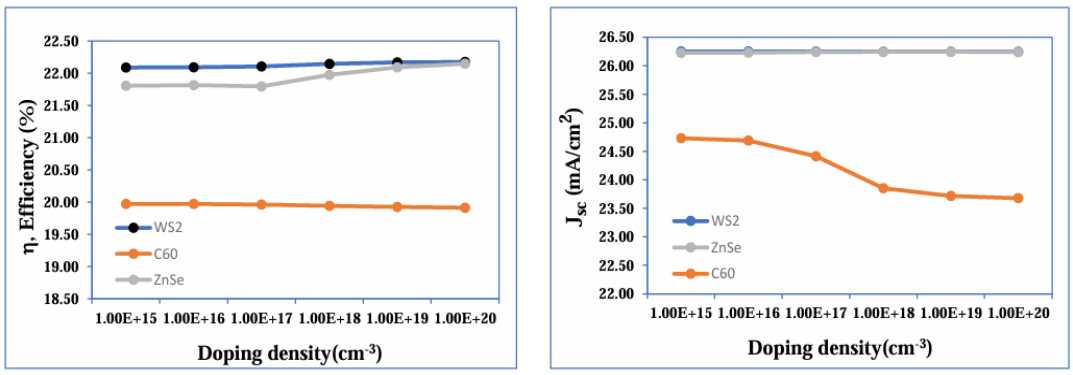

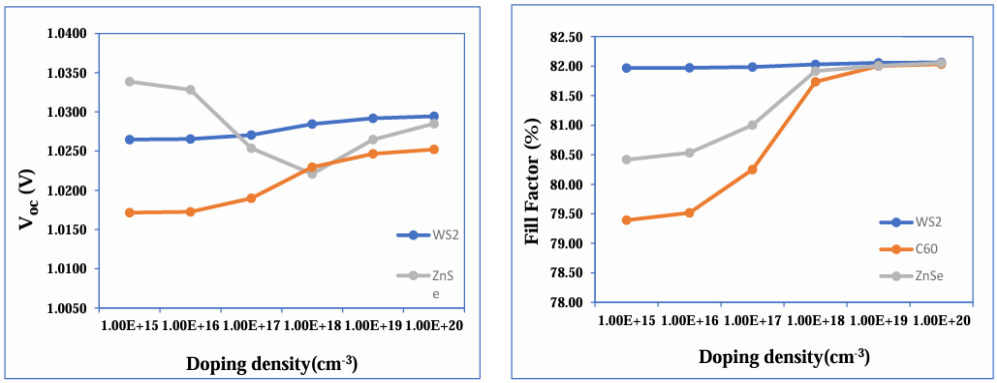

Fig. 8: Effect of ETL doping concentration on PV output parameters

Influence of ETL Thickness

The thickness of each ETL was varied from 0.03 µm to 0.5 µm with all other parameters fixed as shown in Figure 9. The most striking outcome of this analysis is the divergent response between inorganic and organic ETLs. WS_2 exhibited only a slight reduction in efficiency from 22.09% at 0.03 µm to 21.69% at 0.5 µm, while ZnSe remained virtually flat between 21.82% and 21.75%. C_{60}, however, suffered a catastrophic decline from 19.94% to 5.72% as the layer thickened, accompanied by a JSC collapse from 23.85 to 7.21 mA/cm² and a V_{OC} drop from 1.02 to 0.97 V. WS_2 and ZnSe held their JSC values steady (≈ 26.2 mA/cm²) and their V_{OC} fixed at 1.02 V across the full range. FF showed similarly modest variations for the inorganic stacks (WS_2: 81.97% → 81.06%; ZnSe: 80.99–81.27%), but C_{60} degraded from 81.73% to 81.27%. This sharp sensitivity of C_{60} to thickness arises from its low electron mobility (8×10^{-2} cm²/V·s), which causes an exponential rise in transport resistance and recombination losses with increasing path length. By contrast, WS_2 and ZnSe with electron mobilities two to three orders of magnitude higher — sustain efficient electron extraction even in moderately thick layers. From a fabrication standpoint, this finding implies that ETL thickness control is far more critical when adopting organic ETLs, whereas the inorganic alternatives offer a wider processing latitude.

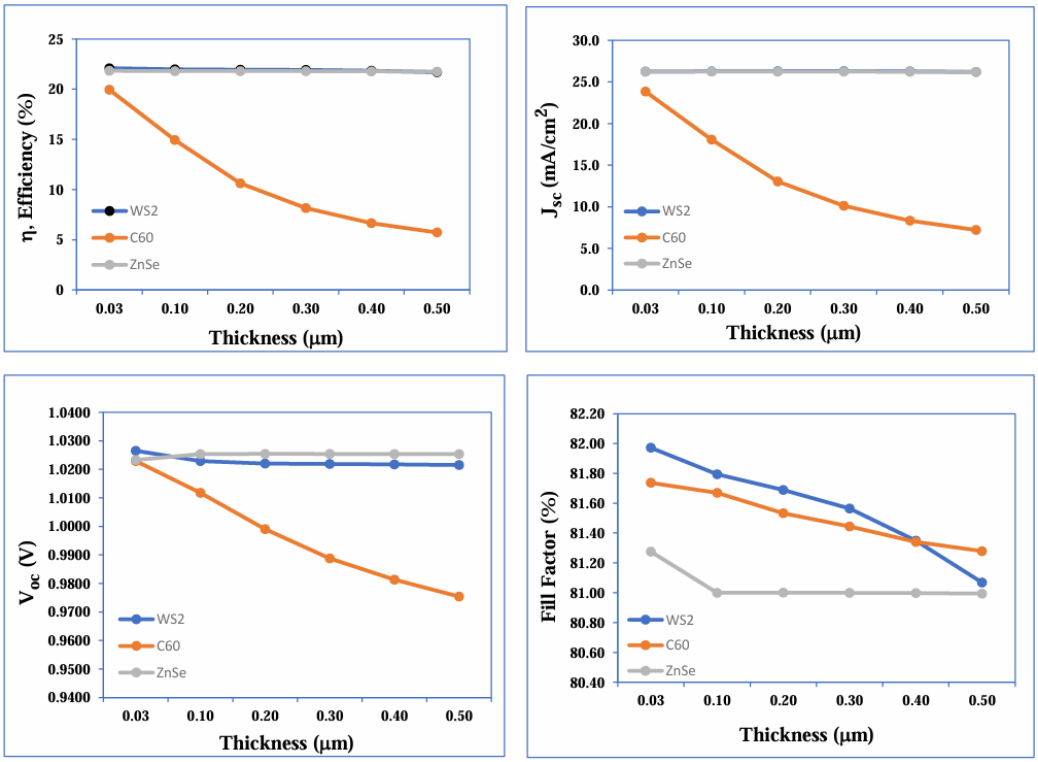

Fig. 9: Influence of ETL thickness variation on PV output parameters

Effect of Hole Transport Layer (CBTS) Parameters

Influence of HTL Defect Density

The CBTS defect concentration was varied between 10^{12} and 10^{18} cm^{-3} to evaluate its impact on device output as shown in Figure 10. A striking result emerges: The photovoltaic metrics of all three devices remained essentially unaffected by HTL defect density across the entire sweep. WS_2 retained η of 22.09%, JSC of 26.25 mA/cm², V_{OC} of 1.02 V, and FF of 81.97%; ZnSe held η of 21.79%, J_{SC} of 26.24 mA/cm², V_{OC} of 1.02 V, and FF of 81.00%; and C_{60} stabilised at η of 19.94%, J_{SC} of 23.85 mA/cm², and V_{OC} of 1.02 V. The insensitivity of device output to CBTS trap states reflects the favourable valence-band alignment between CBTS and $CsSnCl_3$, which keeps interfacial recombination minimal even in the presence of bulk HTL defects. This finding has practical implications, suggesting that fabrication tolerance on the HTL side is comparatively forgiving a useful attribute when scaling up device manufacture.

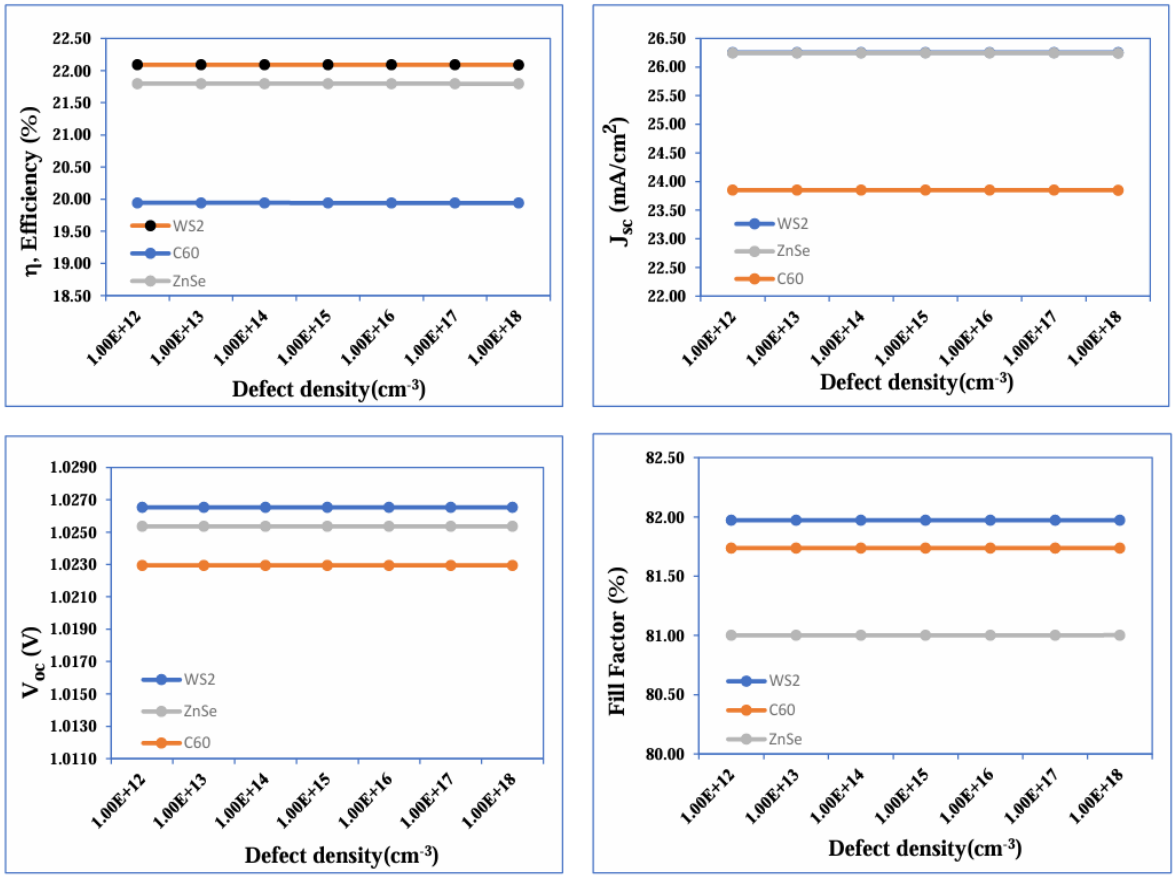

Fig. 10: Variation of PV output parameters with CBTS defect density for the three ETL configurations

Influence of HTL Doping Density

The CBTS acceptor concentration was swept from 10^{15} to 10^{21} cm^{-3}, with the resulting device response presented in Figure 11. In contrast to the defect-density analysis, HTL doping produced clear improvements in performance. The WS_2-based device experienced the largest gain in efficiency, climbing from 21.53% to 22.12%, while ZnSe progressed from 21.42% to 21.82% and C_{60} improved more modestly from 19.43% to 19.97%. Marginal increases in JSC accompanied this trend (WS_2: 26.18 → 26.25 mA/cm²; ZnSe: Peak 26.24 mA/cm²; C_{60}: 23.74 → 23.85 mA/cm²), with VOC stabilised at 1.02 V across all configurations. The most pronounced improvements appeared in FF: WS_2 rose from 80.97% to 82.01%, ZnSe from 80.49% to 81.03%, and C_{60} from 80.86% to 81.77%. The mechanism is straightforward heavier HTL doping reduces series resistance at the absorber/HTL interface and strengthens the built-in field, both of which improve hole extraction without imposing the recombination penalty that often accompanies excessive absorber doping. Optimising the CBTS doping level therefore represents a low-risk, high-reward strategy for performance enhancement.

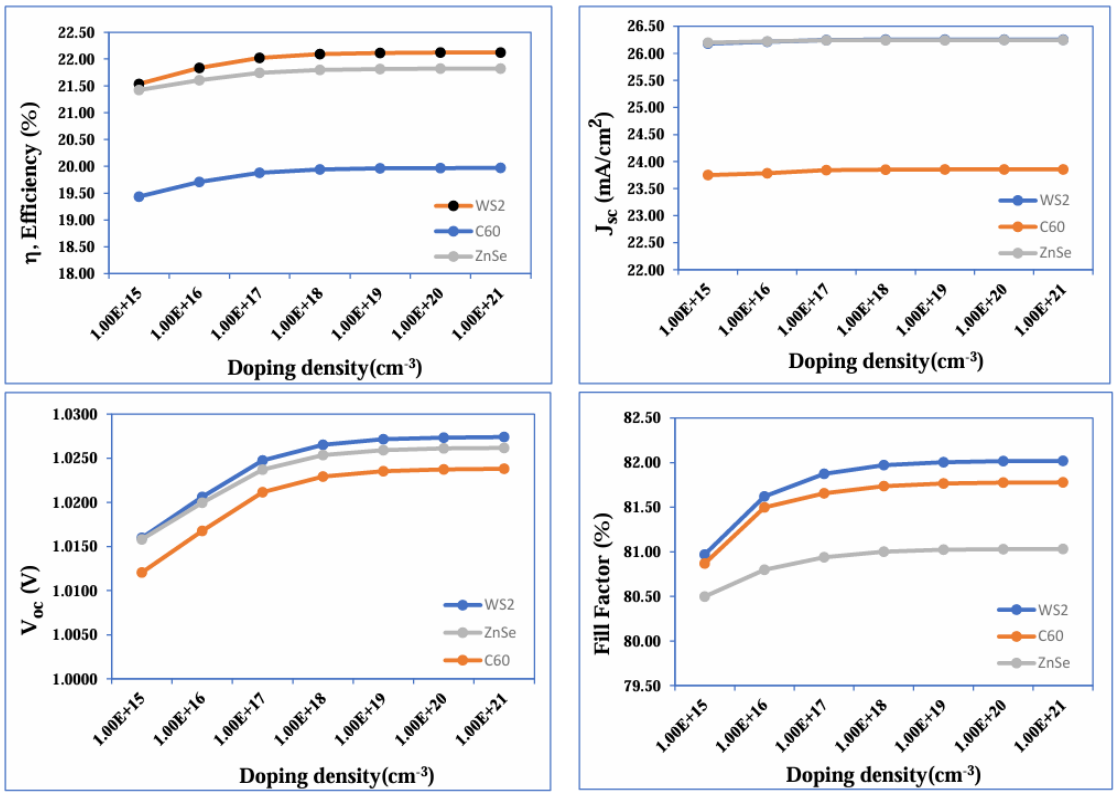

Fig. 11: Effect of CBTS doping concentration on PV output parameters

Influence of HTL Thickness

CBTS thickness was varied between 0.03 µm and 0.5 µm; the resulting trends are summarised in Figure 12. Across the swept range, the device output proved remarkably stable. C_{60} exhibited a tiny rise from 21.79% to 21.81%, ZnSe varied between 19.93% and 19.96%, and WS_2 progressed marginally from 22.08% to 22.10%. The corresponding JSC values increased only slightly (WS_2: 26.24 → 26.27 mA/cm²; C_{60}: 26.23 → 26.26 mA/cm²; ZnSe: 23.84 → 23.87 mA/cm²), while VOC remained constant at 1.02 V and FF stabilised near 81.97%, 81.00%, and 81.73% for WS_2, C_{60}, and ZnSe, respectively. This insensitivity arises from the high hole mobility of CBTS (10 cm²/V·s), which permits efficient hole transport even across modest path lengths, combined with the negligible parasitic absorption loss that CBTS introduces. The result implies that CBTS layer thickness can be tuned over a broad window during fabrication without compromising device output.

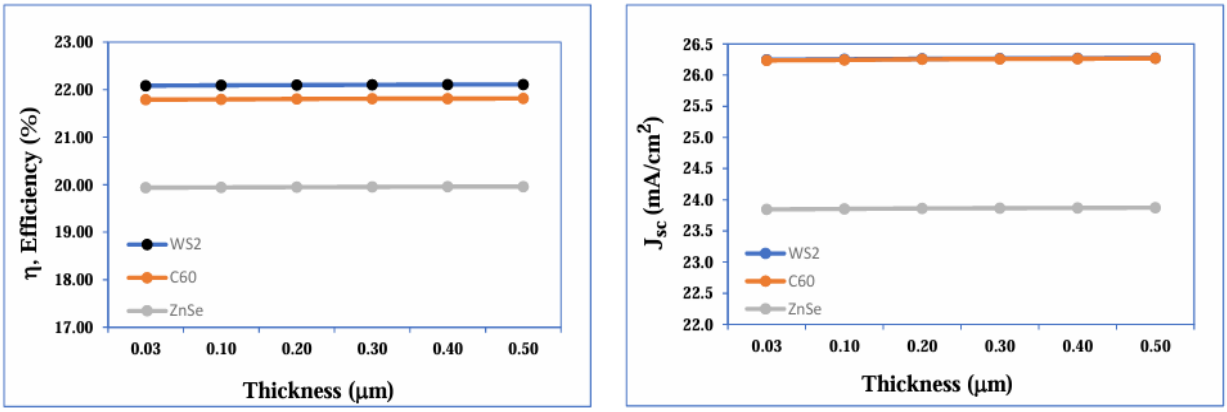

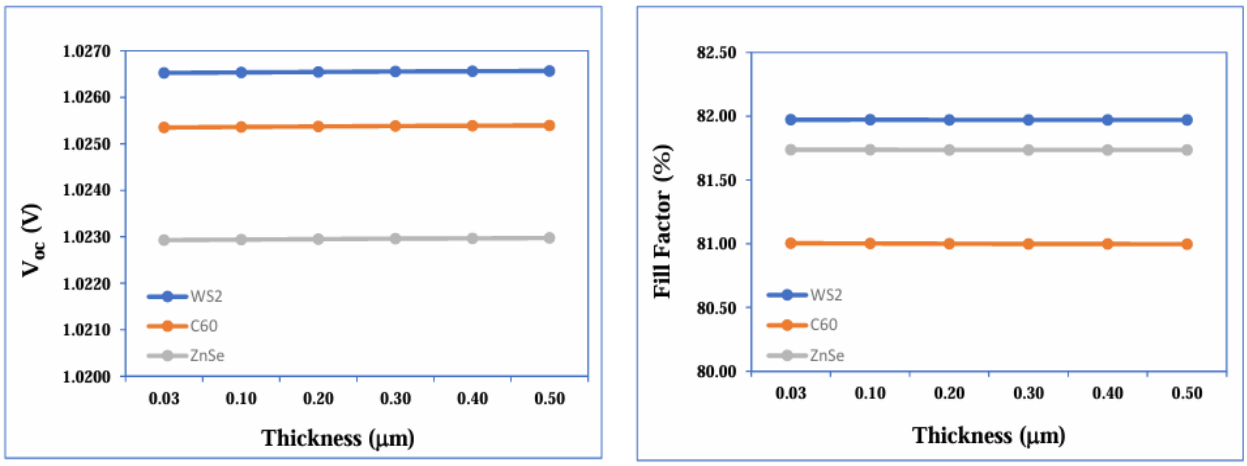

Fig. 12: Influence of HTLs (CBTS) thickness variation on PV output parameters

Capacitance and Mott–Schottky Analysis

The capacitance–voltage (C–V) and Mott–Schottky (M–S) responses were extracted at a probe frequency of 1 MHz to suppress contributions from deep-level traps, with the bias voltage swept between –0.8 V and +0.8 V as shown in Figure 13 and 14. The C–V curves displayed an exponential rise under increasing forward bias for all three configurations, signalling charge accumulation as the depletion layer narrows toward the absorber thickness. At +0.8 V, the ZnSe-based stack exhibited the highest capacitance, followed by WS_2 and then C_{60}. Under reverse bias, the capacitance dropped sharply for all devices, reflecting the broadening of the depletion region and the increase in saturation current. The non-linear nature of the curves together with the multiple intersections among the three configurations indicates that interfacial properties of each ETL/absorber junction differ noticeably.

The Mott–Schottky plots provide complementary information regarding the built-in potential (V_bi) and the dopant ionisation profile through the slope of the $1/C^2$ versus V relationship. A steeper slope is conventionally associated with lower trap density, while a shallower slope indicates a higher concentration of charged interface states. In the present study, the M–S slopes flattened with increasing forward bias for all three devices, in agreement with previously reported behaviour of perovskite-based heterojunctions. The relative ordering observed across the three ETLs is consistent with the JSC and VOC trends already established in earlier subsections, confirming that the inorganic-ETL devices benefit from cleaner interfacial physics than their organic counterpart.

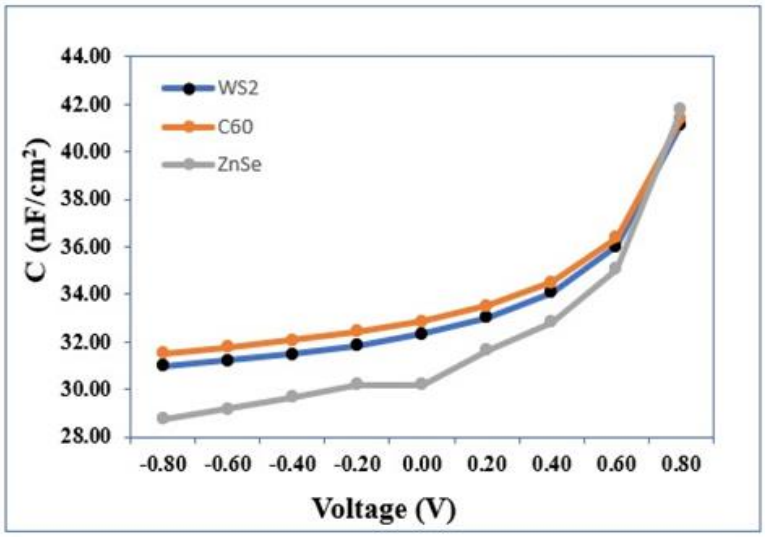

Fig. 13: C–V profile for all ETL configurations

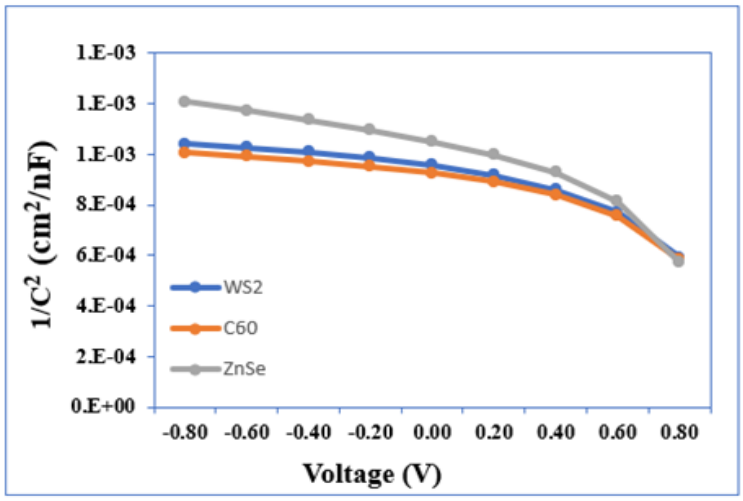

Fig. 14: Mott-Schottky profile

Generation and Recombination Profiles

Carrier generation and recombination rates were extracted along the absorber thickness for the three optimised configurations presented in Figure 15 (a) and (b). Each device exhibits distinct generation behaviour as a function of bias. WS_2 displayed an oscillatory generation rate, beginning at 9.04 units at 0 V, dipping to 2.72 at 0.2 V, recovering to 5.88 at 0.4 V, and then declining to 2.03 at 1 V. C_{60} followed a comparable trajectory, starting at 8.83, peaking near 5.76, and ultimately falling to 2.03. The ZnSe-based device, by contrast, started at a lower value of 1.02 units at 0 V before rising sharply to a maximum of 6.18 at 0.4 V, indicating that its charge generation is more strongly bias-activated than the others.

Recombination profiles revealed that WS_2 and C_{60} began with high recombination rates of 2.59×10^{15} and 2.53×10^{15} units, respectively, at 0 V, which steadily decreased with increasing bias. ZnSe registered the highest initial recombination rate of 2.94×10^{15} units at 0 V but maintained more uniform recombination behaviour at elevated biases — a feature suggestive of improved carrier extraction once the device is brought into operating conditions. Taken together, the generation–recombination analysis indicates that WS_2 and C_{60} favour intermediate bias operation, whereas ZnSe offers superior generation activity and recombination stability at higher biases, opening the possibility of tailoring each device toward bias-specific applications.

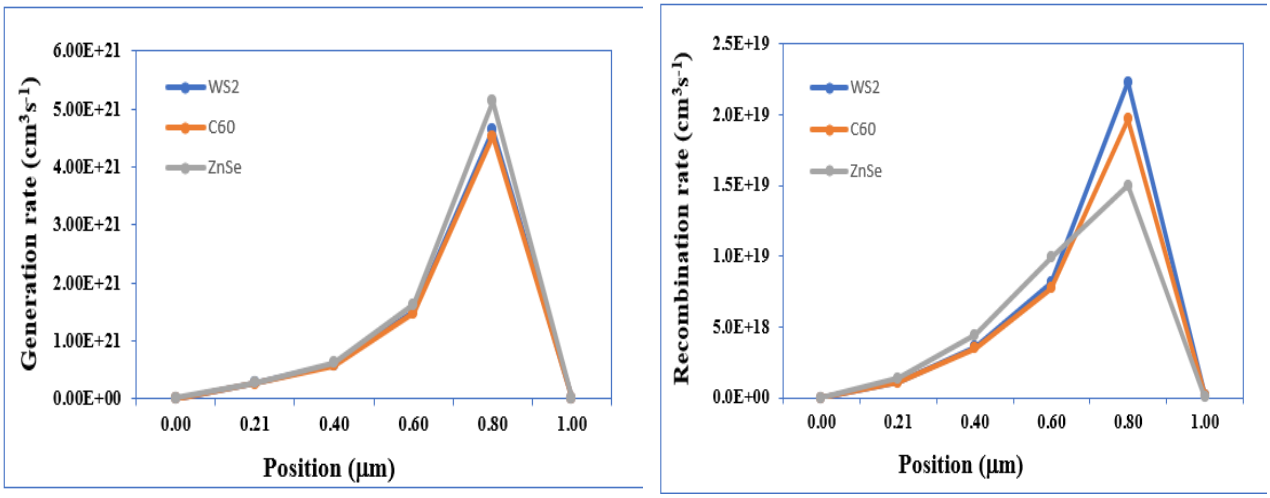

Fig. 15: (a) Generation Rate and (b) Recombination Rate Distribution for all ETLs

Comparative Photovoltaic Performance Across ETL and HTL Configurations

The optimized photovoltaic figures of merit for the $CsSnCl_3$-based devices, evaluated across the ETL and HTL combinations studied, are compiled in Tables 4.

Among the ETL screening shown in Table 4, the WS_2-based device claims the top position with $\eta = 22.09\%$, VOC = 1.03 V, JSC = 26.25 mA/cm², and FF = 81.97%. ZnSe trails by a narrow margin at $\eta = 21.80\%$, while C_{60} delivers a markedly lower 19.94% efficiency, primarily because of its low electron mobility and the resulting susceptibility to recombination. On the HTL side (Table 4), CBTS consistently outperforms CuI and CuO when combined with the WS_2 ETL, registering the highest fill factor and short-circuit current density. The CuI variant suffers from the lowest VOC (1.00 V) and FF (79.48%), reflecting suboptimal energy-level alignment with $CsSnCl_3$, while CuO offers a competitive but slightly inferior outcome. The overall optimum configuration therefore corresponds to ITO/WS_2/$CsSnCl_3$/CBTS/Au, which strikes the most favourable balance of all four photovoltaic metrics — establishing it as the principal device candidate identified in this study.

Conclusion

In the present work, a thorough numerical exploration of a lead-free $CsSnCl_3$-based PSCs was conducted with the SCAPS-1D, and the central objective of finding an efficient, environmentally sustainable, device architecture. Three candidates of ETL, namely WS_2, C_{60} and ZnSe, were systematically benchmarked against three alternatives of HTL (CBTS, CuI, and CuO) within the Glass/ITO/ETL/$CsSnCl_3$/HTL/Au framework, and performance was compared with published reports on similar devices. Based on the screening exercise, the ITO/WS_2/$CsSnCl_3$/CBTS/Au stack was the most promising configuration showing open-circuit voltage of 1.03 V, short-circuit current density of 26.25 mA/cm^2, a fill factor of 81.97 and a power conversion efficiency of 22.09. The ZnSe based and C_{60} based architectures obtained PCEs of 21.80% and 19.94% respectively, and the relative performance of each could be attributed to differences in carrier mobility, conduction-band alignment, and tolerance to interfacial defects. In addition to the headline efficiency, a wide range of operation and physical factors had been addressed in the study: The bulk parameters of the absorber (thickness, acceptor doping, and defect density), the corresponding parameters of both the ETL and the HTL, the operating temperature and the series and shunt resistances. Complementary analyses of capacitance-voltage behaviour and Mott-Schottky response, current density-voltage characteristics, quantum efficiency and the spatial profiles of carrier generation and recombination all provided a coherent picture of how each design lever influences device output. The optimized structure also exhibited good quantum efficiency over the visible and near-infrared spectrum and the inferred covalent nature of the SnCl bonds - supported by considerations of charge density - underlines the favourable optoelectronic behaviour of the CsSnCl3 absorber. In the future, the current research results should help in the current quest to create lead-free photovoltaic platforms that are both sustainable and mechanically as well as operationally sound. In particular, the proposed ITO/WS_2/$CsSnCl_3$/CBTs/Au architecture gives a plausible blueprint for further experimental validation and scaling, and the broader screening framework adopted here may be readily extended to other emerging absorber chemistries other than $CsSnCl_3$.

Acknowledgment

Thank you to the publisher for their support in the publication of this research article. We are grateful for the resources and platform provided by the publisher, which have enabled us to share our findings with a wider audience. We appreciate the efforts of the editorial team in reviewing and editing our work, and we are thankful for the opportunity to contribute to the field of research through this publication.

Funding Information

The authors have no support or funding to report.

Author's Contributions

Rony Tota: Conceptualization, methodology, simulation, formal analysis, supervision, project administration, original draft preparation.

Shak Mahmudul Hasan: Literature review, data interpretation, and writing review and edited.

Md. Morsalin: Manuscript review support.

Md. Muien Ahmed Arnob: Parameter selection, simulation calibration, and data visualization.

Tarikul Islam Tasin: Data curation, simulation support, validation, writing review and edited.

Md. Zamil Sultan: CAPS-1D modeling assistance, graphical representation, and results analysis, critical revision of the manuscript.

Ethics

This article is original and contains unpublished material. The corresponding author confirms that all of the other authors have read and approved the manuscript and no ethical issues involved.

References

Ahmad, W., Noman, M., Tariq Jan, S., & Khan, A. D. (2023). Performance analysis and optimization of inverted inorganic CsGeI perovskite cells with carbon/copper charge transport materials using SCAPS-1D. *Royal Society Open Science*, *10*(3), 221127. https://doi.org/10.1098/rsos.221127

Arumugam, G. M., Karunakaran, S. K., Liu, C., Zhang, C., Guo, F., Wu, S., & Mai, Y. (2021). Inorganic hole transport layers in inverted perovskite solar cells: A review. *Nano Select*, *2*(6), 1081–1116. https://doi.org/10.1002/nano.202000200

Burgelman, M., Nollet, P., & Degrave, S. (2000). Modelling polycrystalline semiconductor solar cells. *Thin Solid Films*, *361–362*, 527–532. https://doi.org/10.1016/s0040-6090(99)00825-1

Chakraborty, R., Sim, K. M., Shrivastava, M., Adarsh, K. V., Chung, D. S., & Nag, A. (2019). Colloidal Synthesis, Optical Properties, and Hole Transport Layer Applications of Cu_2BaSnS_4 (CBTS) Nanocrystals. *ACS Applied Energy Materials*, *2*(5), 3049–3055. https://doi.org/10.1021/acsaem.9b00473

Chapin, D. M., Fuller, C. S., & Pearson, G. L. (2011). Solar energy conversion. *Physics Today*, *60*(3), 37–42.

Chowdhury, M. S., Shahahmadi, S. A., Chelvanathan, P., Tiong, S. K., Amin, N., Techato, K., Nuthammachot, N., Chowdhury, T., & Suklueng, M. (2020). Effect of deep-level defect density of the absorber layer and n/i interface in perovskite solar cells by SCAPS-1D. *Results in Physics*, *16*, 102839. https://doi.org/10.1016/j.rinp.2019.102839

Green, M. A., Ho-Baillie, A., & Snaith, H. J. (2014). The emergence of perovskite solar cells. *Nature Photonics*, *8*(7), 506–514. https://doi.org/10.1038/nphoton.2014.134

Jiang, Y., Li, J., Zhao, Y., Yin, J., & Tang, H. (2020). Theoretical insights into the structural and optoelectronic properties of CsSnCl3 perovskite: A lead-free photovoltaic material. *Journal of Alloys and Compounds*, *852*, 156879.

Leijtens, T., Eperon, G. E., Noel, N. K., Habisreutinger, S. N., Petrozza, A., & Snaith, H. J. (2015). Stability of Metal Halide Perovskite Solar Cells. *Advanced Energy Materials*, *5*(20), 1500963. https://doi.org/10.1002/aenm.201500963

Li, H., Huang, Y., Zhu, M., Yan, P., & Sheng, C. (2025). Analyzing Efficiency of Perovskite Solar Cells Under High Illumination Intensities by SCAPS Device Simulation. *Nanomaterials*, *15*(4), 286. https://doi.org/10.3390/nano15040286

Niemegeers, A., Gillis, S., & Burgelman, M. (1998). A user program for realistic simulation of polycrystalline heterojunction SCs: SCAPS 1D. *Proc. 2nd World Conf*, 672–675.

Park, N.-G. (2015). Perovskite SCs: an emerging photovoltaic technology. *Materials Today*, *18*(2), 65–72. https://doi.org/https://doi.org/10.1016/j.mattod.2014.07.007

Saidani, O., Khirouni, K., Ghribi, M., Allagui, N., Alshareef, H., & Chouchene, R. (2023). An extensive study on multiple ETL and HTL layers to design and simulation of high-performance lead-free CsSnCl3-based perovskite solar cells. *Scientific Reports*, *13*(1), 2521. https://doi.org/10.1038/s41598-023-28506-2

Saliba, M., Matsui, T., Domanski, K., Seo, J.-Y., Ummadisingu, A., Zakeeruddin, S. M., Correa-Baena, J.-P., Tress, W. R., Abate, A., Hagfeldt, A., & Grätzel, M. (2016). Incorporation of rubidium cations into perovskite solar cells improves photovoltaic performance. *Science*, *354*(6309), 206–209. https://doi.org/10.1126/science.aah5557

Simya, O. K., Mahaboobbatcha, A., & Balachander, K. (2015). A comparative study on the performance of Kesterite based thin film solar cells using SCAPS simulation program. *Superlattices and Microstructures*, *82*, 248–261. https://doi.org/10.1016/j.spmi.2015.02.020

Song, Z., McElvany, C. L., Phillips, A. B., Celik, I., Krantz, P. W., Watthage, S. C., Liyanage, G. K., Apul, D., & Heben, M. J. (2017). A technoeconomic analysis of perovskite solar module manufacturing with low-cost materials and techniques. *Energy & Environmental Science*, *10*(6), 1297–1305. https://doi.org/10.1039/c7ee00757d

Ullah, S., Sajjad, M. T., Farooq, M., & Khan, H. A.-H. (2019). Numerical simulation of defect density variation in perovskite SCs using SCAPS. *Results in Physics*, *14*, 102417.

Umar, A., Singh, P. K., Sadanand, Dwivedi, D. K., Ibrahim, A. A., Alhamami, M. A. M., Qasem, H., Akbar, S., & Baskoutas, S. (2022). Design and Simulation of Lead-Free Perovskite Solar Cells with a Hole Transport Layer Made of NiO Nanocomposite. *Science of Advanced Materials*, *14*(9), 1511–1517. https://doi.org/10.1166/sam.2022.4368

Walsh, A. (2015). Principles of Chemical Bonding and Band Gap Engineering in Hybrid Organic–Inorganic Halide Perovskites. *The Journal of Physical Chemistry C*, *119*(11), 5755–5760. https://doi.org/10.1021/jp512420b